



# Mechanical Properties and Cracking Behavior in Single-Fractured Sandstone under Triaxial Compression



Lili Wu<sup>ORCID</sup>, Liming Zhang<sup>\*ORCID</sup>

School of Civil Engineering, Qingdao University of Technology, 266520 Qingdao, China


\* Correspondence: Liming Zhang ([dryad.274@163.com](mailto:dryad.274@163.com))

**Received:** 11-16-2023

**Revised:** 12-28-2023

**Accepted:** 01-07-2024

**Citation:** L. L. Wu and L. M. Zhang, “Mechanical properties and cracking behavior in single-fractured sandstone under triaxial compression,” *GeoStruct. Innov.*, vol. 2, no. 1, pp. 1–9, 2024. <https://doi.org/10.56578/gsi020101>.

 © 2024 by the author(s). Published by Acadlore Publishing Services Limited, Hong Kong. This article is available for free download and can be reused and cited, provided that the original published version is credited, under the CC BY 4.0 license.

**Abstract:** In rock masses, internal defects such as joints, faults, and fractures are pivotal in determining mechanical behavior and structural integrity. This investigation, employing the discrete element numerical simulation technology of GDEM, examines the mechanical attributes of single-fractured sandstone under standard triaxial compression. The study focuses on how fracture inclination angle and confining pressure affect crack propagation within the rock. It is observed that an increase in both fracture inclination angle and confining pressure correlates with a reduction in the tensile stress growth rate near the fracture, indicative of inhibited crack propagation. A notable transition in the failure mode of the sandstone samples is identified, shifting from tensile-shear to predominantly shear failure. This shift is more pronounced under varying confining pressures: Low confining pressure conditions show a prevalence of tensile-shear damage units in proximity to the fracture, while high confining pressure leads to a dominance of shear damage units. These findings contribute to a deeper understanding of fracture mechanics in rock materials and have significant implications for geological and engineering applications where rock stability is critical.

**Keywords:** Fractured rock mass; GDEM computational method; Crack propagation; Failure mode

## 1 Introduction

In the realm of major engineering projects, such as mining, transportation, and energy, rock masses form the fundamental construction environment. These masses, shaped by extensive geological tectonic activities, are characterized by a variety of defects including cavities, joints, faults, and fractures [1–4]. The presence of these defects, and fractures in particular, imparts significant heterogeneity, discontinuity, and anisotropy to the rock masses, profoundly influencing their mechanical behavior [5–8].

Internationally, considerable research has been devoted to understanding the failure mechanisms within fractured rock masses [9–11]. Yang et al. [12] investigated the impact of high-temperature conditions on the triaxial mechanical failure behavior of sandstone with a solitary fracture. It was discovered that as temperature escalated, parameters such as crack closure stress, nucleation stress, and damage threshold exhibited an initial increase followed by a decrease. Liu et al. [13] conducted experimental studies on the mechanical properties of single-fractured sandstone under triaxial extension, observing a transition in the failure stress of the samples from tensile to compressive as confining pressure increased, alongside a shift in microscopic fracture mode from intergranular to transgranular fracturing. In a study by Fujii and Ishijima [14], uniaxial compression tests on cement mortar with an inclined fracture revealed that fracture initiation occurred at the tip, with the primary crack extension direction correlating with the concentration of compressive stress at this point. Wu et al. [15] examined the behavior of pseudo-rock materials containing filled twist fractures under uniaxial tensile failure and identified two distinct failure modes: tip failure and non-tip failure.

Physical model experiments, serving as a direct means to investigate the mechanical properties and crack propagation in fractured rock, are hampered by challenges such as elevated sample costs and lengthy durations. In response, numerical simulation methods have gained prominence, offering the ability to perform multiple calculations at reduced costs and to establish diverse boundary conditions, thus proving instrumental in examining the strength failure processes in defective rock. Finite element methods, as utilized by Song et al. [16] and Yang et al. [17], have been employed to analyze rock samples with fractures, unveiling a linear relationship between uniaxial compressive strength and deformation modulus in fractured rock. However, the discontinuous nature of rock poses a challenge for

traditional numerical simulation methods in replicating the internal characteristics of rock. In contrast, the discrete element method (DEM) aptly captures the non-linearity, heterogeneity, and anisotropy of rock materials [18]. Wang et al. [19] leveraged PFC2D in their study of crack coalescence patterns and microcrack propagation in uniaxially compressed fractured sandstone, discovering that an increase in fracture inclination leads to a decrease in tensile macroscopic cracks and an increase in shear cracks at the point of sample failure. Similarly, Vasarhelyi and Bobet [20] implemented the FROCK program to simulate the effects of uniaxial compression on pseudo-rock materials, noting the origination of wing cracks and secondary cracks from the fracture tips.

Conventional numerical simulation methods often fall short in accurately depicting the progressive failure patterns of rock masses and in reflecting the non-uniform, discontinuous nature of rock materials. Among the existing discrete element computational methods, PFC particle flow DEM software emerges as a primary tool. Despite its efficacy, this software presents challenges in terms of unclear physical parameter meanings and complex parameter calibration. Moreover, scholar-developed programs frequently lack versatility, being apt for only specific cases. This study introduces a novel discrete element computational method, GDEM, enhanced with GPU acceleration, to simulate both the micro-mechanical properties and macroscopic cracking behavior of rock containing a single fracture under conventional triaxial compression.

## 2 Construction of Numerical Model for Single-Fractured Sandstone

For an in-depth analysis of the fracturing mechanism in rocks with fractures and to visually capture the entire process of rock deformation and failure, GDEM is employed. This discrete element software proficiently replicates the complete deformation and failure process of rock. Utilizing this approach, the intrinsic mechanical behavior and macroscopic crack propagation patterns in fractured rock are analyzed.

### 2.1 Overview of GDEM Software

GDEM, an advanced numerical simulation software, operates on the Continuous Discontinuous Element Method (CDEM) principle. Optimized for multi-core central processing unit (CPU) parallel processing and explicit dynamics, GDEM builds upon the generalized Lagrangian equations as its mathematical foundation. This integration of finite and discrete elements facilitates a comprehensive simulation approach. The GDEM numerical model, as illustrated in Figure 1, enables the simulation of structural deformation, stress-strain behavior within each specimen, and the crack propagation process [21].

### 2.2 Computational Principles of GDEM Software

The GDEM software is predicated on the generalized Lagrange and variational formulations. Its core computational model is based on the mass-spring system, which serves as the iterative foundation (Figure 2), effectively capturing material interface characteristics via crack propagation and penetration. In instances of tensile failure within a block, separation characteristics are exhibited, while shear failure results in the block displaying sliding characteristics [21]. The failure criteria for the spring model within this framework are delineated as follows.

### 2.3 Boundary Conditions for the Numerical Model

Informed by the experimental findings of Liu et al. [4], a cylindrical two-dimensional numerical model, dimensions 50 mm by 100 mm, was developed. This model incorporated a single edge crack at inclination angles of 30°, 45°, and 60°. Triangular elements were employed for mesh division within the model, with the grid division for the 45° fracture specifically depicted in Figure 3.

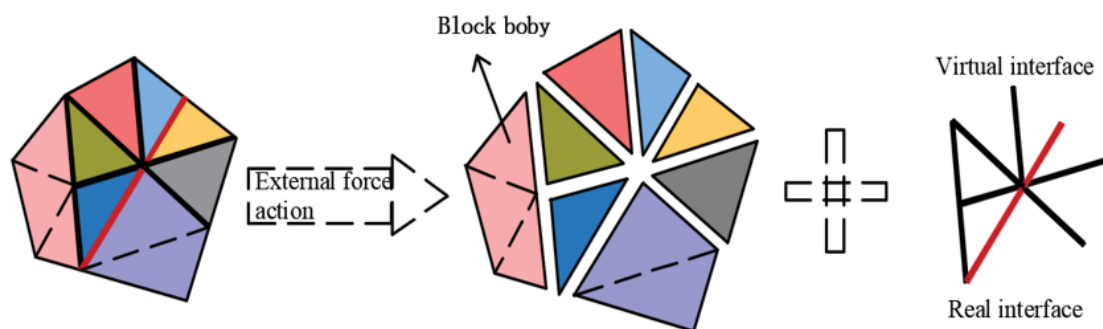


**Figure 1.** Composition of the GDEM numerical model

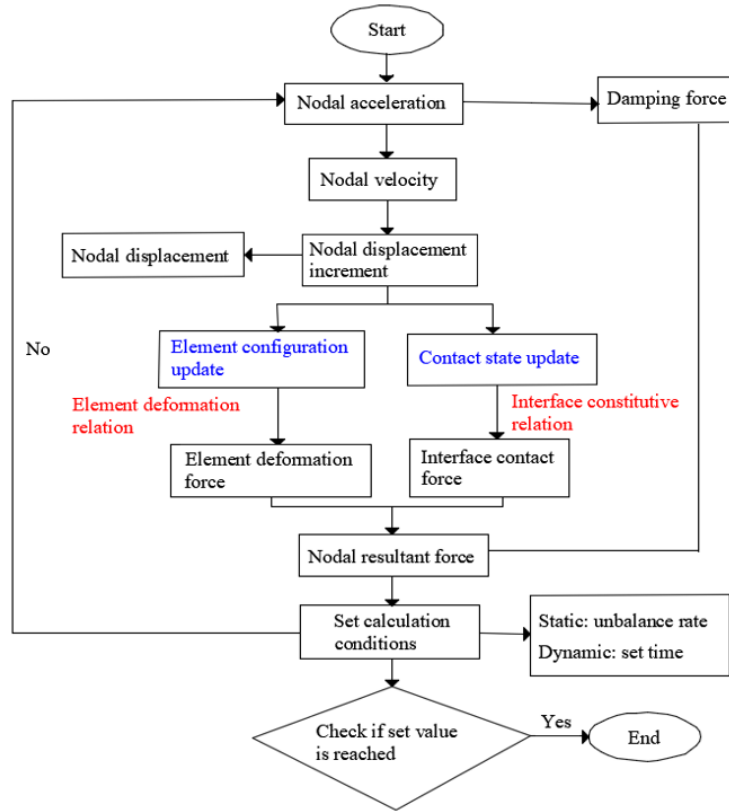


**Figure 2.** Iterative process of block dyna

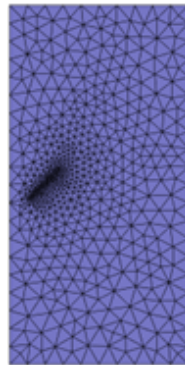


**Figure 3.** Diagram of grid division

**Table 1.** Basic physical and mechanical parameters

Density/(kg · m <sup>-3</sup> )	Elastic Modulus/(MPa)	Poisson's Ratio	Internal Friction Angle/(°)	Cohesion/(MPa)	Tensile Strength/(MPa)
2600	5e <sup>10</sup>	0.26	30	3e <sup>6</sup>	3e <sup>6</sup>

A normal constraint was applied to the base of the numerical model. Simultaneously, varying magnitudes of confining pressure were exerted on the lateral aspects. Quasi-static displacement loading was executed along the y-axis. Furthermore, the interaction between material blocks in the model was represented using a semi-spring model. The failure criterion for each unit within this setup adhered to the Mohr-Coulomb criterion, while the contact surface model for the blocks was established as an elastic-brittle model. The simulation employed a displacement-controlled loading approach, proceeding at a rate of  $2e^{-6} \text{ m}\cdot\text{s}^{-1}$ . Reflecting the physical parameters and experimental outcomes obtained from laboratory tests on sandstone, the foundational physical and mechanical parameters deployed in the numerical simulation are outlined in Table 1.

## 2.4 Experimental Configurations and Simulation Process

For the simulation, a comprehensive numerical model was developed, incorporating a single fracture depicted as a rigid line of 12 mm length, illustrated in Figure 4. Varied schemes were established based on differing fracture inclinations and confining pressures, detailed in Table 2.

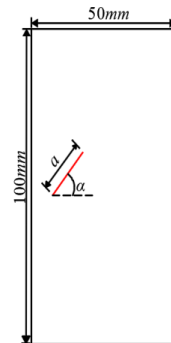


**Figure 4.** Diagram of single fracture distribution

**Table 2.** Experimental configurations

Scheme Number	Fracture Inclination Angle/ °	Confining Pressure/MPa
1	30	0
		5
		15
2	45	0
		5
		15
3	60	0
		5
		15

## 3 Analysis of Specimen Failure Behavior

### 3.1 Analysis of Crack Propagation Behavior

Informed by prior research, the predominant crack propagation types observed in specimens with a single fracture are delineated in Figure 5 [4]. These types include tensile wing cracks, antithetic wing cracks, secondary shear cracks, primary shear cracks, splay cracks, and far-field cracks. Subsequent to conventional triaxial compression, the numerical simulation results, illustrating macroscopic damage in the specimens, are depicted in Figure 6.

Figure 6 presents the numerical simulation outcomes of macroscopic damage in single fracture specimens under various fracture inclination angles (represented by black lines). It was observed that the samples predominantly exhibited mixed tensile-shear failure when  $\alpha=\beta=30^\circ$ . At lower confining pressures, tensile wing cracks initially emerged at the left tip of the fracture, with primary shear cracks forming at the right tip. As the loading progressed, these primary shear cracks extended upwards, culminating in a petal-like pattern at the top of the specimen. Conversely, under higher confining pressures, the development of wing cracks was notably restrained, leading to an increase in both secondary and far-field cracks due to enhanced lateral constraints. In cases of shear failure when  $\alpha=\beta=45^\circ$ , distinct behavioral patterns were noted depending on the confining pressure. Under low confining pressure, significant tensile wing cracks were observed at the left tip of the fracture, accompanied by antithetic wing cracks expanding into reverse shear cracks at the right tip. With elevated confining pressure, the fracture's left tip exhibited multiple bifurcating tensile cracks alongside nucleated tensile wing cracks, attributable to increased lateral constraint. This phenomenon led to the specimens predominantly undergoing shear failure  $\alpha=\beta=60^\circ$ . Notably, under high confining pressure, pronounced antithetic wing cracks developed at the right tip of the fracture, extending and expanding towards the specimen's base. These simulation results are in robust agreement with findings from conventional triaxial compression tests conducted in laboratory settings [4], affirming the validity of the numerical model and its applicability in understanding fracture mechanics in rock materials.

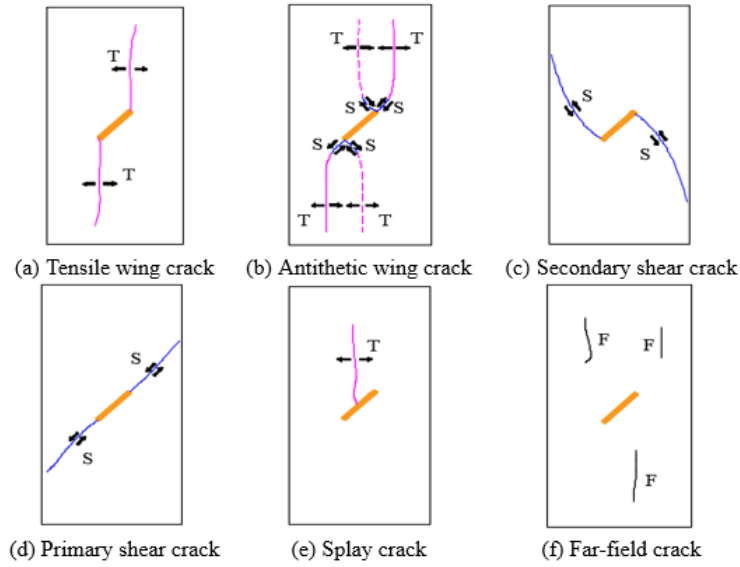


Figure 5. Classification of crack propagation in single fracture specimens [4]

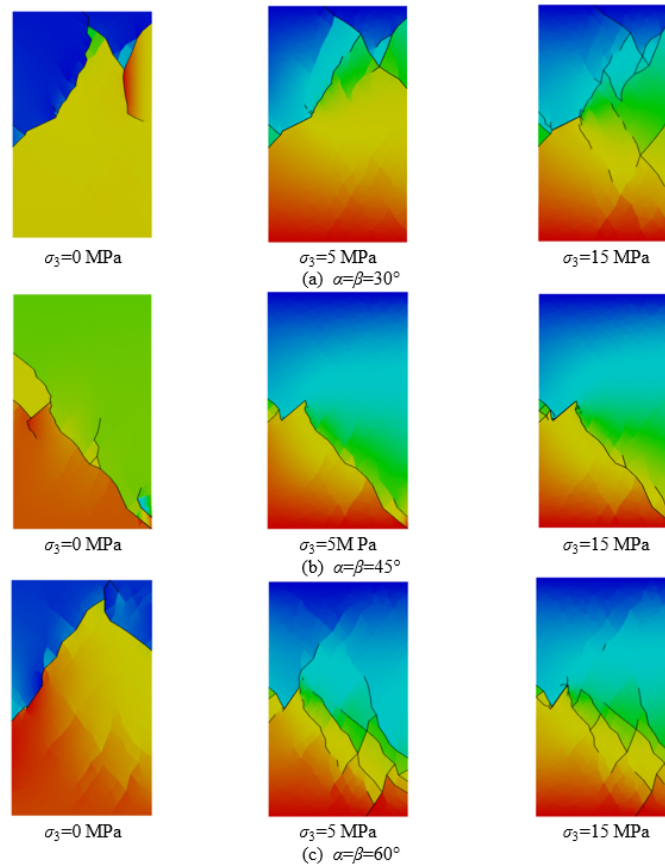


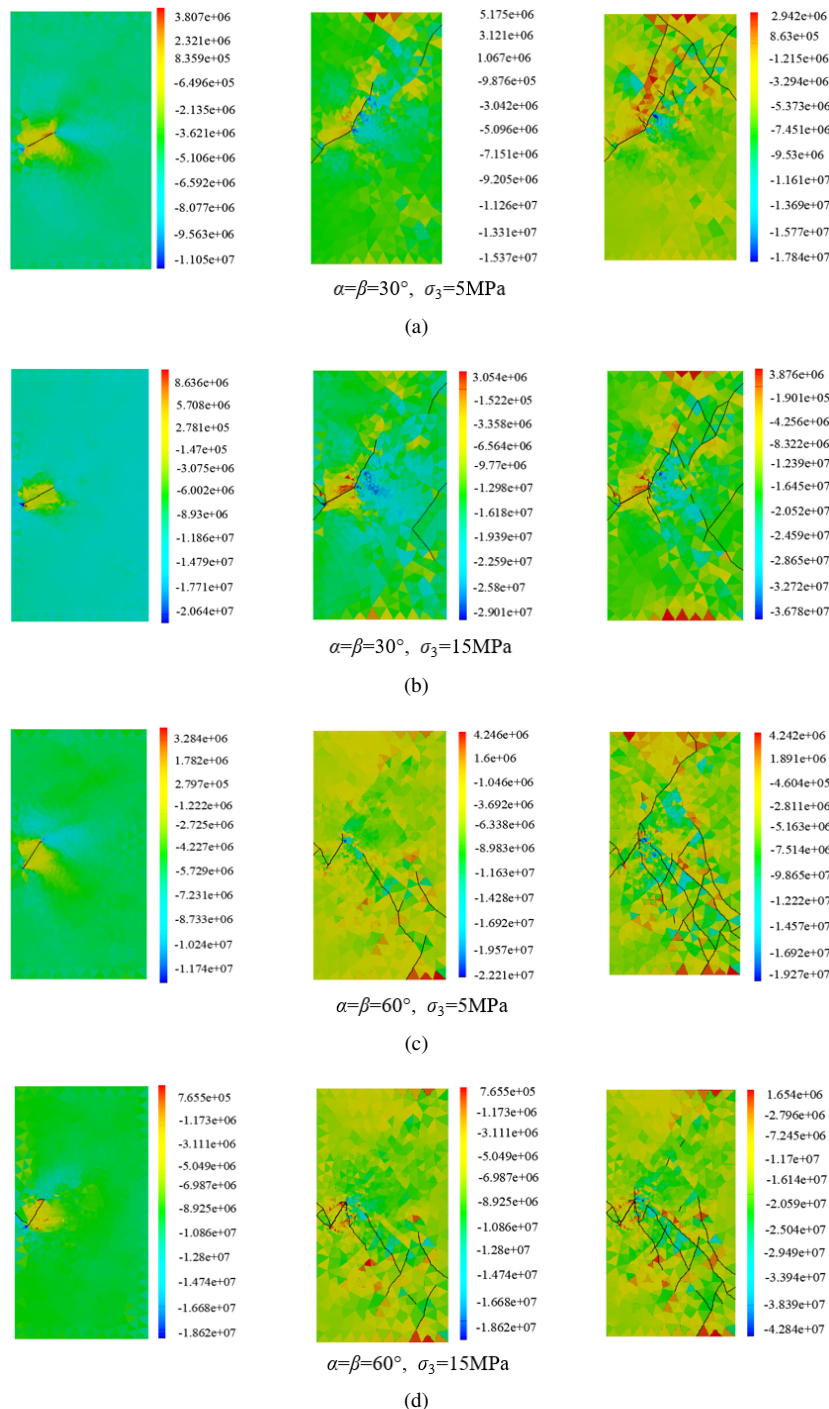
Figure 6. Macroscopic damage results in simulation

### 3.2 Stress Field Evolution in Fractured Specimens

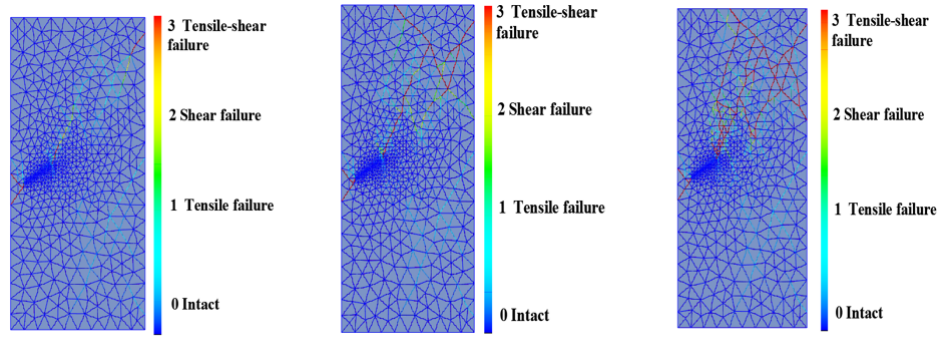
Figure 7 illustrates the stress field evolution in specimens subjected to conventional triaxial compression. This segment of the study specifically examines specimens with fracture inclination angles of  $30^\circ$  and  $60^\circ$ , subjected to both low and high confining pressures of 5 MPa and 15 MPa, respectively.

Figure 7 provides a visual depiction of the stress field cloud maps for specimens under diverse crack inclination angles and confining pressure conditions. In scenarios where  $\alpha=\beta=30^\circ$  and  $\sigma_3=5$  MPa, it was observed that the maximum stress value in the specimen during loading experienced a gradual increase from 3.81 MPa to 5.12 MPa

and subsequently to 6.94 MPa. This pattern signifies a concentration of stress at the crack tip, denoted by the red area, progressively leading to the formation of a tensile stress zone. At this juncture, crack nucleation and expansion commence from the tip, culminating in tensile-shear failure. For specimens with  $\alpha=\beta=30^\circ$  and  $\sigma_3=15$  MPa, there was an increase in the maximum stress value from 3.65 MPa to 5.88 MPa and then to 8.64 MPa. While a tensile stress zone was also present at the fracture tip, the rise in confining pressure acted to inhibit the expansion of tensile wing cracks. In the case of  $\alpha=\beta=60^\circ$  and  $\sigma_3=5$  MPa, the maximum stress value during loading rose from 3.28 MPa to 4.24 MPa, and further to 5.25 MPa. Lastly, for  $\alpha=\beta=60^\circ$  and  $\sigma_3=15$  MPa, the maximum stress value escalated from 3.59 MPa to 5.69 MPa and finally to 7.66 MPa. These findings indicate that with ongoing loading, tensile stress develops at the crack ends, leading to increased crack nucleation. Concurrently, the growth of tensile wing cracks is constrained, resulting in the specimen predominantly undergoing shear failure.

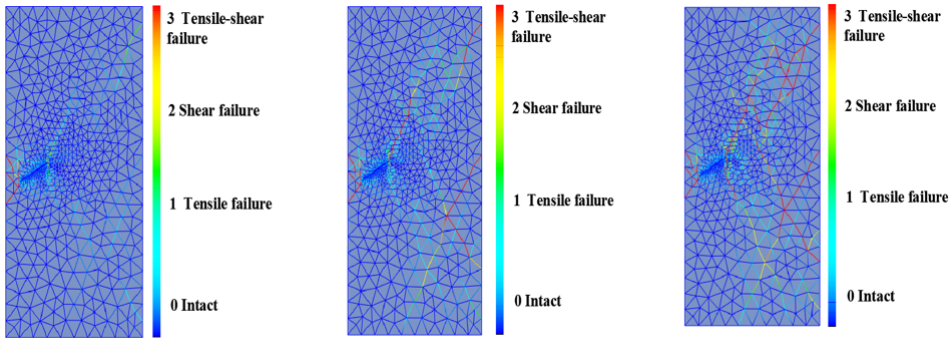


**Figure 7.** Stress field cloud map of specimens under different crack inclination angle and confining pressure conditions



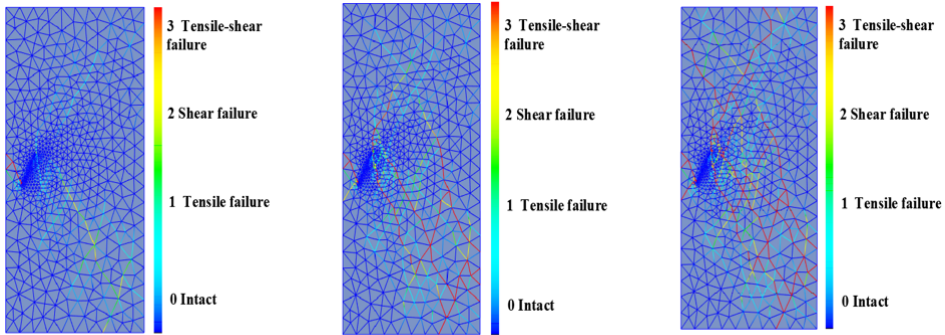
$$\alpha=\beta=30^\circ, \sigma_3=5 \text{ MPa}$$

(a)



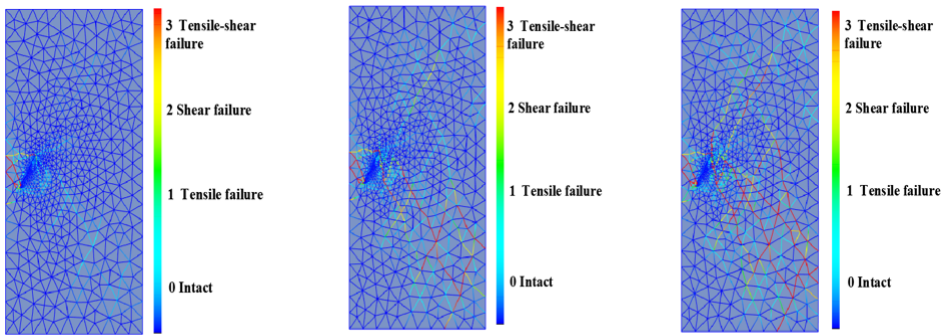
$$\alpha=\beta=30^\circ, \sigma_3=15 \text{ MPa}$$

(b)



$$\alpha=\beta=60^\circ, \sigma_3=5 \text{ MPa}$$

(c)



$$\alpha=\beta=60^\circ, \sigma_3=15 \text{ MPa}$$

(d)

**Figure 8.** Failure modes of specimens under different crack inclination angle and confining pressure

### 3.3 Evolution of Failure Modes

Figure 8 presents cloud maps that elucidate the failure modes of specimens under varying fracture inclination angles and confining pressure conditions. In cases where  $\alpha=\beta=30^\circ$  and  $\sigma_3$  is 5 MPa and 15 MPa, a marked stress concentration is observed at the fracture tip during the loading process. This phenomenon initiates cracking at the fracture tip, with a progressive increase in the number of tensile-shear damage units (indicated as numbers 2 and 3) near the tip, ultimately penetrating to the edge of the specimen. As confining pressure escalates, there is a notable reduction in the quantity of yellow-red tensile-shear damage units near the crack, while an increase in shear damage units (indicated as number 1) is observed, leading to a tensile-shear failure mode in the specimen. Conversely, when  $\alpha=\beta=60^\circ$  and  $\sigma_3$  is 5 MPa and 15 MPa, the extension of shear damage units from the tip along the fracture direction towards the edge is evident, resulting in a predominant shear failure mode. Additionally, within these specimens, an increased presence of far-field cracks and more dispersed shear damage units is detected.

### 4 Conclusions

It has been observed that the stress field patterns within single fracture rock exhibit significant variations under different fracture inclination angles and confining pressure conditions. Specifically, at a  $30^\circ$  fracture inclination angle under low confining pressure, stress concentration at the fracture tip leads to the nucleation of cracks and the subsequent formation of a tensile stress zone within a defined range. Conversely, at high confining pressure, the extent of tensile stress in proximity to the fracture tip is reduced. For fracture angles inclined at  $60^\circ$ , the imposition of low confining pressure results in the formation of tensile stress zones at both ends of the fracture, predominantly manifesting as primary shear cracks. At elevated confining pressures, a diminishing growth of tensile stress near the fracture is noted.

Furthermore, distinct crack propagation behaviors and failure modes are discernible in single fracture rock, contingent upon the fracture inclination angle and confining pressure conditions. With a fracture inclination angle of  $30^\circ$  under low confining pressure, the specimen predominantly exhibits tensile-shear failure, characterized by a considerable presence of tensile-shear damage units near the fracture tip. At higher confining pressures, the specimen tends towards shear failure, marked by an increased prevalence of shear damage units near the crack. At a  $60^\circ$  fracture inclination angle, shear failure is observed, where shear damage units indicative of such failure extend along the fracture direction to the edge of the specimen.

### Data Availability

The data used to support the research findings are available from the corresponding author upon request.

### Conflicts of Interest

The authors declare no conflict of interest. The funders analyzed and interpreted some of the data in the design of the study.

### References

- [1] Z. X. Tian, W. S. Zhang, C. Q. Dai, B. L. Zhang, Z. Q. Ni, and S. J. Liu, "Permeability model analysis of combined rock mass with different lithology," *Arab. J. Geosci.*, vol. 12, no. 24, p. 755, 2019. <https://doi.org/10.1007/s12517-019-4951-6>
- [2] B. G. He, R. Zelig, Y. H. Hatzor, and X. T. Feng, "Rockburst generation in discontinuous rock masses," *Rock Mech. Rock Eng.*, vol. 49, no. 10, pp. 4103–4124, 2016. <https://doi.org/10.1007/s00603-015-0906-8>
- [3] J. Z. Zhang, H. Y. Qiu, Y. B. Cao, and B. L. Li, "Triggering of rockburst in layered composite rocks," *Arab. J. Geosci.*, vol. 15, no. 15, p. 1336, 2022. <https://doi.org/10.1007/s12517-022-10642-0>
- [4] X. R. Liu, "Study on the mechanical behavior and failure mechanism of fissured rock under triaxial compression," Ph.D. dissertation, China University of Mining and Technology, 2021. <https://doi.org/10.27623/d.cnki.gzkyu.2020.002489>
- [5] L. M. Zhang, D. Zhang, Z. Q. Wang, Y. Cong, and X. S. Wang, "Constructing a three-dimensional creep model for rocks and soils based on memory-dependent derivatives: A theoretical and experimental study," *Comput. Geotech.*, vol. 159, p. 105366, 2023. <https://doi.org/10.1016/j.compgeo.2023.105366>
- [6] P. H. S. W. Kulatilake, S. Wang, and O. Stephansson, "Effect of finite size joints on the deformability of jointed rock in three dimensions," *Int. J. Rock Mech. Min. Sci. Geomech. Abstr.*, vol. 30, no. 5, pp. 479–501, 1993. [https://doi.org/10.1016/0148-9062\(93\)92216-D](https://doi.org/10.1016/0148-9062(93)92216-D)
- [7] H. L. Liu, X. H. Feng, L. Y. Liu, T. J. Li, and C. N. Tang, "Mechanical properties and failure characteristics of anisotropic shale with circular hole under combined dynamic and static loading," *Int. J. Rock Mech. Min. Sci.*, vol. 170, p. 105524, 2023. <https://doi.org/10.1016/j.ijrmms.2023.105524>



- [8] E. Z. Lajtai, "Strength of discontinuous rocks in direct shear," *Géotechnique*, vol. 19, no. 2, pp. 218–233, 1969. <https://doi.org/10.1680/geot.1969.19.2.218>
- [9] L. M. Zhang, X. S. Wang, Y. Cong, Z. Q. Wang, and J. Liu, "Transfer mechanism and criteria for static–dynamic failure of granite under true triaxial unloading test," *Geomech. Geophys. Geo-Energy Geo-Resour.*, vol. 9, no. 1, p. 104, 2023. <https://doi.org/10.1007/s40948-023-00645-w>
- [10] L. M. Zhang, W. W. Chao, Z. Y. Liu, Y. Cong, and Z. Q. Wang, "Crack propagation characteristics during progressive failure of circular tunnels and the early warning thereof based on multi-sensor data fusion," *Geomech. Geophys. Geo-Energy Geo-Resour.*, vol. 8, p. 172, 2022. <https://doi.org/10.1007/s40948-022-00482-3>
- [11] H. J. Wang, H. L. Liao, W. L. Niu, J. M. Peng, and Y. H. He, "Comparative analysis of impact failure modes between slotted rock and intact rock," *Geothermics*, vol. 114, p. 102801, 2023. <https://doi.org/10.1016/j.geothermics.2023.102801>
- [12] S. Q. Yang, B. Hu, and W. L. Tian, "Effect of high temperature damage on triaxial mechanical failure behavior of sandstone specimens containing a single fissure," *Eng. Fract. Mech.*, vol. 233, p. 107066, 2020. <https://doi.org/10.1016/j.engfracmech.2020.107066>
- [13] Z. L. Liu, C. D. Ma, X. A. Wei, and W. B. Xie, "Experimental study on the mechanical characteristics of single-fissure sandstone under triaxial extension," *Rock Mech. Rock Eng.*, vol. 55, no. 7, pp. 4441–4457, 2022. <https://doi.org/10.1007/s00603-022-02876-x>
- [14] Y. Fujii and Y. Ishijima, "Consideration of fracture growth from an inclined slit and inclined initial fracture at the surface of rock and mortar in compression," *Int. J. Rock Mech. Min. Sci.*, vol. 41, no. 6, pp. 1035–1041, 2004. <https://doi.org/10.1016/j.ijrmms.2004.04.001>
- [15] Y. L. Wu, Q. Q. Dong, J. He, and Q. Y. Chen, "Performance of rock-like materials containing filled kinked fissures under uniaxial tension at failure," *KSCE J. Civ. Eng.*, vol. 27, no. 3, pp. 1205–1223, 2023. <https://doi.org/10.1007/s12205-023-0864-8>
- [16] J. Song, M. Dong, S. Koltuk, H. Hu, L. Q. Zhang, and R. Azzam, "Hydro-mechanically coupled finite-element analysis of the stability of a fractured-rock slope using the equivalent continuum approach: A case study of planned reservoir banks in blaubeuren, germany," *Hydrogeol. J.*, vol. 26, no. 3, pp. 803–817, 2018. <https://doi.org/10.1007/s10040-017-1694-x>
- [17] J. P. Yang, W. Z. Chen, D. S. Yang, and J. Q. Yuan, "Numerical determination of strength and deformability of fractured rock mass by fem modeling," *Comput. Geotech.*, vol. 64, pp. 20–31, 2015. <https://doi.org/10.1016/j.compgeo.2014.10.011>
- [18] B. Vásárhelyi and A. Bobet, "Modeling of crack initiation, propagation and coalescence in uniaxial compression," *Rock Mech. Rock Eng.*, vol. 33, no. 2, pp. 119–139, 2000. <https://doi.org/10.1007/s006030050038>
- [19] Y. Q. Wang, K. Peng, X. Y. Shang, L. P. Li, Z. P. Liu, Y. Wu, and K. Long, "Experimental and numerical simulation study of crack coalescence modes and microcrack propagation law of fissured sandstone under uniaxial compression," *Theor. Appl. Fract. Mech.*, vol. 115, p. 103060, 2021. <https://doi.org/10.1016/j.tafmec.2021.103060>
- [20] B. Vasarhelyi and A. Bobet, "Modeling of crack initiation, propagation and coalescence in uniaxial compression," *Rock Mech. Rock Eng.*, vol. 33, no. 2, pp. 119–139, 2000. <https://doi.org/10.1007/s006030050038>
- [21] Y. Song, Z. H. Luo, B. Zhang, Y. Zhang, and M. Zhu, "Effect of fracture location on failure modes of short columns under uniaxial compression," *J. Shandong Univ. (Eng. Sci.)*, vol. 53, no. 5, pp. 121–131, 2023. <https://doi.org/10.6040/j.issn.1672-3961.0.2022.163>